International Journal of Solids and Structures 128 (2017) 282–295

Contents lists available at ScienceDirect

International Journal of Solids and Structures

journal homepage: www.elsevier.com/locate/ijsolstr

Multiscale modeling of cemented tungsten carbide in hard rock drilling

Dmitry Tkalich[a,b], Vladislav A. Yastrebov[a,*], Georges Cailletaud[a], Alexandre Kane[c]

[a] MINES ParisTech, PSL Research University, Centre des Matériaux, CNRS UMR 7633, BP 87, 91003 Évry cedex, France
[b] Norwegian University of Science and Technology (NTNU), Sem Sælands veg 1 NO-7491 Trondheim, Norway
[c] SINTEF Materials and Chemistry, Materials and Nanotechnology, Richard Birkelandsvei 2, NO-7465 Trondheim, Norway

ARTICLE INFO

Article history:
Received 1 October 2016
Revised 17 August 2017
Available online 1 September 2017

Keywords:
Cemented tungsten carbide
Microstructure
Homogenization
Multiscale simulation
Uniform field model
Beta-model
Finite element analysis
Yield surface
Impact
Drilling

ABSTRACT

Mechanical behavior of rotary-percussive drilling tools made of tungsten carbide (WC) hardmetal in impact interaction with hard rock is investigated. This study presents a three-step multiscale simulation strategy, developed for evaluation of stress and strain heterogeneity within the hardmetal microstructure when subjected to loadings representative for drilling applications. Two homogenization approaches are used: a full-field finite-element model and a Beta-model (a nonlinear extension of the Kröner's uniform field model). Both models combine isotropic Drucker–Prager elasto-plastic behavior of WC grains and isotropic von Mises elasto-plastic behavior of the binder, and include nonlinear hardening. First, a three-dimensional finite-element model of a representative volume element is constructed, which closely resembles the hardmetal microstructure. Full-field simulation with applied proportional loadings allows to determine the hardmetal effective elastic properties for different binder content, and an initial yield surface, resembling in shape a Drucker–Prager surface with a cap. These simulations are also used to calibrate the Beta-model, which, however, cannot predict the correct plastic behavior for the loadings with high hydrostatic component. Second, macroscopic finite-element simulations of normal and oblique frictional impact of an elastic rock by a hardmetal spherical tip are performed using a macroscopic set-up. The calibrated Beta-model is used at every Gauss-point of the hardmetal impactor. Finally, the most critical for the hardmetal's integrity points are identified on the impactor's surface, and complex non-proportional stress paths associated with these points are extracted. These stress paths are used as boundary conditions in a full-field simulations employing representative volume elements of hardmetal microstructure. Analysis of stress and plastic-strain fields at the microstructural scale suggests that the major source of wear of drilling inserts may come from tensile failure of WC grains.

1. Introduction

Rotary-percussive drilling is the main method when penetrating hard rock formations. Rock crushing is achieved by repetitive impacts and flushing out the rock debris. Majority of drill-bits are constructed of spherically-tipped cylindrical WC hardmetal inserts embedded in a metallic "crown" - see Fig. 1a. WC hardmetal inserts (black in Fig. 1a and b) are the main operating components of the drill-bit, which come in contact with rock. Wear of the hardmetal inserts leads to loss of drill-bit's functional shape and increasing expenses related to the drill-bit replacement. WC hardmetal is a dual-phase composite, where ceramic brittle Tungsten Carbide grains with a high strength in compression are embedded in metallic matrix - the binder (Fang and Koopman, 2014). Material used as a binder is usually Cobalt, Nickel, Iron and their mixes, with binder content ranges from 5 to 20 vol.%. Different combinations of hardness and toughness properties for this composite are achieved by varying mainly binder content and composition, and WC grain size.

The aim of this paper is to illustrate, by numerical simulation, the heterogeneity of the stress and strain fields within the microstructure, induced by the representative stresses acting on the hardmetal during drilling. In order to achieve the above, the following steps are taken. (i) The effective (average) behavior of the hardmetal is obtained by means of a homogenization method based on a direct 3D finite-element simulation of a representative volume element (RVE). A uniform field (UF) model, based on Eshelby's solution of the inclusion problem, extended to elasto-plasticity is calibrated to reproduce closely the behavior of the RVE model. (ii) The finite element (FE) simulation of an impact

* Corresponding author.
E-mail address: vladislav.yastrebov@mines-paristech.fr (V.A. Yastrebov).

http://dx.doi.org/10.1016/j.ijsolstr.2017.08.034

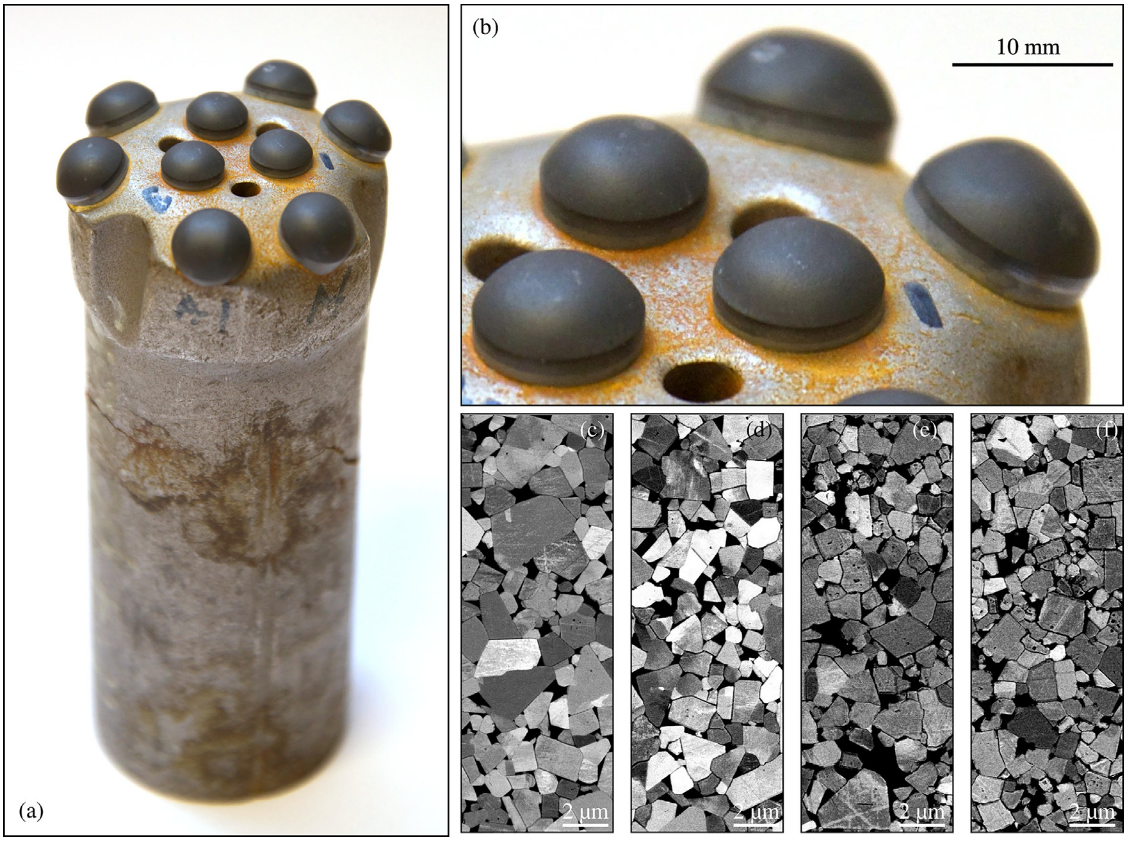

Fig. 1. (a)Typical drill-bit for percussive drilling with nine WC hardmetal inserts, (b) close-up of worn drill-bit insert, (c)–(f) scanning electron microscope images of different WC hardmetal grades.

of a spherical WC hardmetal impactor and the rock formation is performed. The UF model obtained in the previous step is used in the macro-scale simulations. (iii) A selection of stress histories is extracted from critical material points of the hardmetal in the impact simulations. Such stress paths, representative of those acting on the hardmetal insert during drilling, are applied to the 3D RVE models with an explicitly introduced morphology. As a result, we obtain the distribution of stresses and strains within the hardmetal bulk, occurring under loadings, representative for the rotary-percussive drilling.

The two homogenization methods used in the current study are: (i) direct 3D FE simulation of mechanical behavior of the RVE (Kanit et al., 2003; Besson et al., 2009) and (ii) a two-phase UF model with the β-rule (Cailletaud and Pilvin, 1994; Cailletaud and Coudon, 2015) - a nonlinear extension of the classical Kröner's model (Kröner, 1961; Budiansky and WU, 1961). The use of these methods for two-dimensional WC hardmetal models was demonstrated in Tkalich et al. (2017a), showing a good agreement between FE and UF homogenization approaches. All finite-element simulations are performed in Z-set analysis suite (Z-set, 2017). The three-dimensional models with an explicitly introduced microstructural morphology is constructed using Voronoi tessellation algorithm available in Rycroft (2008) with the subsequent subdivision of the created Voronoi grains. An in-depth analysis of the algorithm and of generated microstructures is presented in a separate paper (Yastrebov et al., 2018).

The paper is organized as follows. Constitutive behaviors of the WC and binder phases are presented and discussed in Section 2. The homogenization approaches, together with morphological and numerical aspects of the models and performed simulations are described in Section 3. The results of each step of the strategy are presented consecutively in Section 4. Conclusions are given in Section 5.

2. Materials and constitutive models

Different combinations of toughness and hardness of the WC hardmetal are achieved by adjusting sintering parameters like binder content, binder composition, WC mean grain size and WC grain size distribution. The hardness of the composite is for the most part determined by the tungsten carbide phase, whereas toughness - by the binder phase. Two types of interfaces are present: WC grain–WC grain and WC grain–binder. They also play a significant role in determining overall hardmetal behavior and properties. In compression, macroscopic inelastic deformation in hardmetal can reach 1–3% before fracturing. It originates mainly from the plastic deformation of the ductile binder phase and the formation of stacking faults in WC grains (Roebuck and Almond, 1988). Under bending or tensile loads, a close-to-linear stress-strain dependence is observed up to failure, which occurs usually at strains of 0.1–0.5% (Nishimatsu, 1960; Exner and Gurland, 1970; Jaensson, 1971).

The constitutive equation used for WC and binder phases are presented in the following sections, where material parameters for each phase are chosen according to the data reported in the literature. Variation of constituent materials' properties found in literature give a noticeable scatter. Elastic response of the hardmetal is mostly determined by the WC phase, given its dominant volume fraction. Behavior in plastic regime is determined by the relative shapes of the phases' yield surfaces: binder phase dominates under compressive and shear loadings and WC phase - under tensile. In Tkalich et al. (2017a), the investigation of the sensitivity of the effective hardmetal behavior to the binder plastic properties can

Table 1
Material parameters for elastic and plastic behavior of WC and binder phases.

Tungsten Carbide (WC) grains		
Elastic constants of transversely isotropic WC	C_{11}	720 GPa
	C_{12}	254 GPa
	C_{13}	150 GPa
	C_{33}	972 GPa
	C_{44}	328 GPa
Homogenized isotropic Young's modulus	E_{WC}	707.7 GPa
Homogenized isotropic Poisson's ratio	ν_{WC}	0.197
Initial yield stress in uniaxial compression in Eq. (2)	R_{WC_0}	4 GPa
Friction angle in Eq. (2)	ϕ_{WC}	45°
Dilatation angle in Eq. (4)	ψ_{WC}	30°
Hardening constants in Eq. (3)	Q_{WC}	3 GPa
	b_{WC}	10
Binder, Cobalt		
Young's modulus	E_B	208 GPa
Poisson's ratio	ν_B	0.3
Initial yield stress in Eq. (6)	R_{B_0}	560 MPa
Hardening constants in Eq. (6)	Q_B	607 MPa
	b_B	140

be found, which reports that for the variation of initial yield stress or hardening parameter within a 30% interval, the yield stress in compression changes in the interval of ± 5–6% around the original yield stress.

Interfaces are assumed perfect, as if they are not weakened by defects or impurities. In reality, strength of the WC grain–binder interface, and thus the cohesion of the resulting hardmetal, is determined by the degree of wetting of WC grains by liquid metallic binder (Ramqvist, 1965; Almond and Roebuck, 1988; Pastor, 1999; Gille et al., 2000). WC grain–WC grain bond is determined by both the wetting and energy of the contact for a particular misorientations of adjacent grains. Fracture mechanisms in WC hardmetals are controversial: even the determination of the predominant ones is still under debate. Several numerical studies of crack propagation in the WC hardmetals were carried out in Sigl and Schmauder (1988); Fischmeister et al. (1988); McHugh and Connolly (2003).

2.1. Tungsten carbide

After sintering with metallic binder, tungsten carbide (WC) shapes as convex faceted grains. Its crystal structure has a hexagonal (HCP) unit cell and thus exhibits transversely isotropic elastic behavior (French, 1969; Exner, 1979; Lee and Gilmore, 1982). The elasticity tensor of WC crystals can be defined by five elastic constants. In Voigt notation, it is represented by the following matrix where direction "3" corresponds to the longer axis normal to the HCP basal plane

$$\underset{\sim}{C}_{WC} = \begin{pmatrix} C_{11} & C_{12} & C_{13} & 0 & 0 & 0 \\ \cdot & C_{11} & C_{13} & 0 & 0 & 0 \\ \cdot & \cdot & C_{33} & 0 & 0 & 0 \\ \cdot & \cdot & \cdot & C_{44} & 0 & 0 \\ \cdot & \cdot & \cdot & \cdot & C_{44} & 0 \\ \cdot & \cdot & \cdot & \cdot & \cdot & (C_{11}-C_{12})/2 \end{pmatrix}, \tag{1}$$

where '$\cdot$' stands for symmetrical components. The components of this tensor measured by Lee and Gilmore (1982) and refined by Golovchan and Litoshenko (2010) are listed in Table 1. The isotropic elastic constants were obtained using self-consistent homogenization framework with a model of 2000 randomly oriented grains, assuming a perfect disorder in the material (Kröner, 1977). The resulting values are $E_{WC} = 707.7$ GPa and $\nu_{WC} = 0.197$, which is in good agreement with the experimental measurements (Shackelford et al., 2016). In this study we employ an isotropic elastic behavior for WC grains.

Despite the brittle nature of WC, slip markings are observed in WC grains on the deteriorated surfaces of hardmetal tools (Beste and Jacobson, 2008; Tkalich et al., 2017b). Since, the strength of WC is known to be different in compression and in tension, we used a pressure-dependent Drucker–Prager yield criterion, defined as follows:

$$f_{WC}(\boldsymbol{\sigma}, \bar{p}) = \frac{J_2(\boldsymbol{\sigma}) + I_1(\boldsymbol{\sigma})\tan(\phi_{WC})/3}{1-\tan(\phi_{WC})/3} - R_{WC_0} - Y_{WC}(\bar{p}), \tag{2}$$

where $J_2(\boldsymbol{\sigma}) = \sqrt{\frac{3}{2}\boldsymbol{s}:\boldsymbol{s}}$ is the equivalent (von Mises) stress, $\boldsymbol{s}$ is the deviatoric part of the stress tensor $\boldsymbol{\sigma}$, $I_1(\boldsymbol{\sigma}) = \mathrm{tr}(\boldsymbol{\sigma})$ is the trace of the stress tensor, then the hydrostatic pressure is given by $\mathbb{P} = -\frac{1}{3}\boldsymbol{I}_1(\boldsymbol{\sigma})$ and R_{WC_0} is the initial yield stress for a compression loading and ϕ_{WC} is the friction angle set to 45°. The angle was deduced from the difference in uniaxial tensile and compressive yield stresses identified in Golovchan and Litoshenko (2010). A time independent framework is used, with an isotropic hardening defined as a function of the accumulated plastic strain p

$$Y_{WC}(\bar{p}) = Q_{WC}[1-\exp(-b_{WC}\bar{p})], \text{ with:}$$
$$\bar{p} = \int_0^t \sqrt{\frac{2}{3}\dot{\boldsymbol{\varepsilon}}^p : \dot{\boldsymbol{\varepsilon}}^p}\, d\tau \tag{3}$$

where the plastic strain $\boldsymbol{\varepsilon}^p$ is determined using the total $\boldsymbol{\varepsilon}^{\mathrm{tot}}$ and elastic strain tensors $\boldsymbol{\varepsilon}^e$ by $\boldsymbol{\varepsilon}^p = \boldsymbol{\varepsilon}^{\mathrm{tot}} - \boldsymbol{\varepsilon}^e$, and $\dot{\boldsymbol{\varepsilon}}^p$ denotes its rate. A non-associated flow rule is employed, the flow potential having the following form:

$$g_{WC}(\boldsymbol{\sigma}) = J_2(\boldsymbol{\sigma}) + \frac{1}{3}I_1(\boldsymbol{\sigma})\tan(\psi_{WC}) \tag{4}$$

where ψ_{WC} is the dilatation angle, which defines amount of plastic volumetric strain developed during plastic shearing. We assumed rather arbitrarily $\psi_{WC} = 30°$, as no experimental data were found. For moderate loads, as shown in Section 4, the amount of plastic deformation in WC is rather small, therefore the results are not very sensitive to this parameter. Moreover, one of the key objectives of the study is to obtain the effective yield surface, which is unaffected by the hardening properties. The plastic strain tensor is then calculated, introducing the plastic multiplier $\dot{\lambda}$ to express the constraint, as follows:

$$\dot{\boldsymbol{\varepsilon}}^p = \dot{\lambda}\frac{\partial g_{WC}}{\partial \boldsymbol{\sigma}} \tag{5}$$

with the usual Kuhn–Tucker conditions.

The identification of the material parameters characterizing plastic behavior is based on the available literature, which shows a considerable scatter, attributed to difference in grain size and orientation (Schedler, 1988). The initial yield stress in tension and compression is chosen as an average of those reported in the literature for grain sizes between 5 and 2 μm: 2.0 GPa and 4.0 GPa, respectively (Shatov et al., 2014; Prakash, 2014). The post-yield behavior of WC grains in tension should significantly differ from that in compression: it was found for the basal and prismatic planes, as shown in an experimental study by Csanádi et al. (2014), where uniaxial compression tests on WC micro-pillars were performed. A significantly higher hardening capacity was observed for basal planes compared to the prismatic, which can be attributed to different slip mechanisms. On the one hand, the outer surface of drilling tools undergo large irreversible deformation and micro fracture due to strong stress concentrations originating from the contact with local rock roughness in severe environment (high temperatures and pressures). On the other hand, the difference in slip hardening is not crucial for determining the initial yield surface and for understanding very first stages of plastic flow occurring in drilling applications. Hardening constants are calibrated so that WC grains exhibit post-yield behavior median between those experimentally obtained in Csanádi et al. (2014) for basal and prismatic planes giving the hardening constants $Q_{WC} = 3.0$ GPa and $b_{WC} = 10$. All constants are listed in Table 1.

2.2. Binder

Metallic binder penetrates WC hardmetal bulk in the forms of inter-connected pools and thin channels confined between WC grains. In its “foam”-like structure, the same crystallographic structure of the binder extends, within the composite's bulk, to the distances several times greater than the WC grain sizes. From the scanning electron images of undamaged microstructure it can be seen that the width of binder channels vary and Hall-Petch-like strengthening effect (Hall, 1951; Petch, 1953) takes place due the small mean free paths in some directions and the reduced number of possibly active slip systems. Using the Lee–Gurland model (Lee and Gurland, 1978; Gurland, 1979), we estimated the initial yield stress and work-hardening parameters to be $R_{B_0} = 561.0$ MPa and $Q_B = 607.0$ MPa, respectively. An isotropic elasto-plastic model with a von Mises criterion and isotropic hardening is chosen for the behavior of the binder. The yield surface is defined as

$$f_B(\boldsymbol{\sigma}, \bar{p}) = J_2(\boldsymbol{\sigma}) - R_{B_0} - Y_B(\bar{p}) \qquad \text{with :}$$
$$Y_B(\bar{p}) = Q_B[1 - \exp(-b_B\bar{p})]. \tag{6}$$

Hardening exponent parameter b_B is chosen to be 140. The material parameters are listed in Table 1.

3. Methods

The current section presents the description of three different numerical models and simulations, which are used in the current study within the three-step multiscale strategy described in the introduction. First, geometrical microstructural models constructed using an augmented Voronoi tessellation algorithm are introduced in Section 3.1. Second, analytical uniform field model, based on Eshelby's solution of inclusion problem is recalled and governing equations are provided in Section 3.2. Third, a finite-element model for impact simulation is presented in Section 3.3. The finite-element impact simulation is considered at the macroscopic level: the drill-bit has a centimeter size, and each Gauss point introduces the same constitutive equations. Two models at a lower scale are considered: the UF model represents the average fields in each phase at a meso-scale, which allows us to represent two different phase behaviors, but remains a crude simulation of the RVE; the FE model combines phase behavior and realistic morphology at a micro-scale, and provides the best approach to study the local behavior.

3.1. Geometrical model

Contrary to ordinary two phase composites of matrix/inclusion type, cemented carbides have two types of interfaces: WC grain–WC grain and WC grain–binder. This fact, together with a low volumetric content of the binder phase (5–20% for conventional grades), presents a challenge in generating synthetic realistic morphologies. In the present study the microstructure model is generated using a two step algorithm. First, the Voronoi tessellation is constructed with random seed locations within a cubic box (Barbe et al., 2001; Gérard et al., 2009). Second, each Voronoi grain is cut into two sub-grains by a randomly oriented plane. The position of the cutting plane is chosen such that the volumes of the two sub-grains correspond to the volume fraction of the binder η_B and of the WC $(1-\eta_B)$, i.e. they are $V_0 \cdot (1-\eta_B)$ for the WC and $V_0 \cdot \eta_B$ for the binder, where V_0 is the initial grain volume. Obtained model resembles the real hardmetal morphology composed of WC grains and binder pools (see SEM images in Fig. 1c–e). The algorithm is implemented in the “Voro++” environment, which is freely available (Rycroft, 2008). A detailed morphological study of this model including multiple-cuts option will be presented in a separate paper (Yastrebov et al., 2018).

An example of a finite-element microstructure-respective model consisting of 300 initial Voronoi grains is shown in Fig. 2. Three RVE models with volumetric binder fractions of 7.5, 10 and 15% are shown in Fig. 3, where binder and WC phases are shown separately. The sufficiency of the size of chosen RVE model (corresponding to the volume of approximately $9 \times 9 \times 9\,\mu\text{m}^3$) is assured by (i) isotropy of resulting Young's moduli and Poisson's ratios, (ii) the proximity of elastic tensors obtained using uniform static and kinetic boundary conditions (Hill-Mandel's lemma (Huet, 1990; Besson et al., 2009)) and also (iii) by the fact that different realizations of a random microstructure provide elastic constants, which differ by less than 1%.

3.2. Uniform field model

The specific uniform field model used here is the so called β-rule (Cailletaud and Pilvin, 1994; Cailletaud and Coudon, 2015), which is a nonlinear extension of the classical approach with an elastic accommodation initially introduced by Kröner (1961) and followed by Budiansky and WU (1961). The response of the model includes then the composite's effective curve, as well as responses of each phase. The constitutive equations for the plastic behavior of both phases were presented in Section 2.1 and Section 2.2 with material parameters as given in Table 1. The strain partition writes as follows for each phase

$$\boldsymbol{E} = \underset{\sim}{\mathsf{C}}_{\text{eff}}^{-1} : \boldsymbol{\Sigma} + \boldsymbol{E}^p \ , \ \ \boldsymbol{\varepsilon}_i = \underset{\sim}{\mathsf{C}}_i^{-1} : \boldsymbol{\sigma}_i + \boldsymbol{\varepsilon}_i^p \ , \tag{7}$$

where $\boldsymbol{\Sigma}$ and $\boldsymbol{E}$ are the average stress and strain tensors, respectively, $\boldsymbol{E}^p$ is the macroscopic plastic tensor, $\boldsymbol{\sigma}_i$ and $\boldsymbol{\varepsilon}_i$ are the uniform stress and uniform strain tensors of the ith phase, $\boldsymbol{\varepsilon}_i^p$ is the uniform plastic strain tensors and $\underset{\sim}{\mathsf{C}}_i$ is the fourth order elasticity tensor of the ith phase, and $\underset{\sim}{\mathsf{C}}_{\text{eff}}$ is the macroscopic fourth order elasticity tensor. For the case of significant plastic strain accumulation, a new accommodation variable $\boldsymbol{\beta}_i$ with a nonlinear evolution is introduced in each phase (Cailletaud and Coudon, 2015). This results in the following expression for stresses in each phase “i”:

$$\boldsymbol{\sigma}_i = \underset{\sim}{\mathsf{A}}_i : \left[\boldsymbol{\Sigma} + \underset{\sim}{\mathsf{C}}^\star : (\boldsymbol{\beta} - \boldsymbol{\beta}_i)\right] \ , \tag{8}$$

where $\underset{\sim}{\mathsf{C}}^\star = \underset{\sim}{\mathsf{C}}_{\text{eff}} : (\underset{\sim}{\mathsf{I}} - \underset{\sim}{\mathsf{S}})$, and $\underset{\sim}{\mathsf{S}}$ is the Eshelby tensor, which depends on the shape of the inclusion and on the properties of the homogenized medium, $\underset{\sim}{\mathsf{I}}$ is the fourth-order symmetric unit tensor: $\underset{\sim}{\mathsf{I}} = \frac{1}{2}\left(\delta_i^k\delta_j^l + \delta_i^l\delta_j^k\right)$. The fourth order tensor $\underset{\sim}{\mathsf{A}}_i$ introduces a correction due to the non-uniform elasticity and has the following form:

$$\underset{\sim}{\mathsf{A}}_i = \left[\underset{\sim}{\mathsf{C}}_{\text{eff}} : \underset{\sim}{\mathsf{S}} : \underset{\sim}{\mathsf{C}}_{\text{eff}}^{-1} + \underset{\sim}{\mathsf{C}}^\star : \underset{\sim}{\mathsf{C}}_i^{-1}\right]^{-1}. \tag{9}$$

The second order tensor $\boldsymbol{\beta}_i$ represents the accommodation tensor in each phase and $\boldsymbol{\beta}$ is the corresponding macroscopic tensor. The Eshelby tensor is chosen according to the effective behavior of the material. For the case of a spherical inclusion the expression depends on the effective Poisson's ratio only and reads:

$$\underset{\sim}{\mathsf{S}} = \frac{1}{15(1-\nu_{\text{eff}})}[(5\nu_{\text{eff}} - 1)\boldsymbol{I} \otimes \boldsymbol{I} + 2(4 - 5\nu_{\text{eff}})\underset{\sim}{\mathsf{I}}], \tag{10}$$

where $\boldsymbol{I}$ is the second order identity tensor. Eq. (9) can be rewritten in this case as:

$$\underset{\sim}{\mathsf{A}}_i = \left[\underset{\sim}{\mathsf{S}} + \underset{\sim}{\mathsf{C}}^\star : \underset{\sim}{\mathsf{C}}_i^{-1}\right]^{-1}. \tag{11}$$

The following evolution rules are introduced:

$$\dot{\boldsymbol{\beta}}_i = \dot{\boldsymbol{\varepsilon}}_i^p - ||\dot{\boldsymbol{\varepsilon}}_i^p||\left(D_i^s\boldsymbol{\beta}_i^{\text{sph}}\boldsymbol{I} + D_i^d\boldsymbol{\beta}_i^{\text{dev}}\right) \tag{12}$$

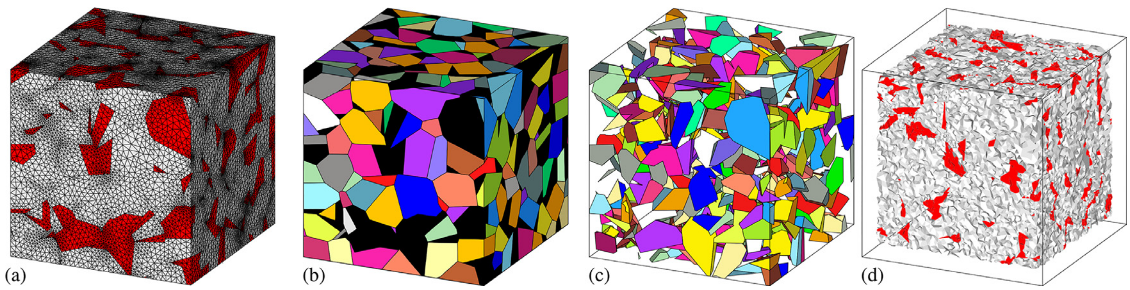

Fig. 2. A model for WC hardmetal microstructure with binder volumetric fraction of 15%: (a) a finite element mesh containing 500 WC grains and 500 binder parts with ≈ 1.6 million elements and 0.27 million nodes, binder phase is shown in red; (b) each color denotes a separate WC grain, while the binder is shown in black; (c) each color denotes a separate binder "grain", WC grains are not shown; (d) an interior 75% volume, over which the statistical study is performed to avoid edge effects. (For interpretation of the references to color in this figure legend, the reader is referred to the web version of this article.)

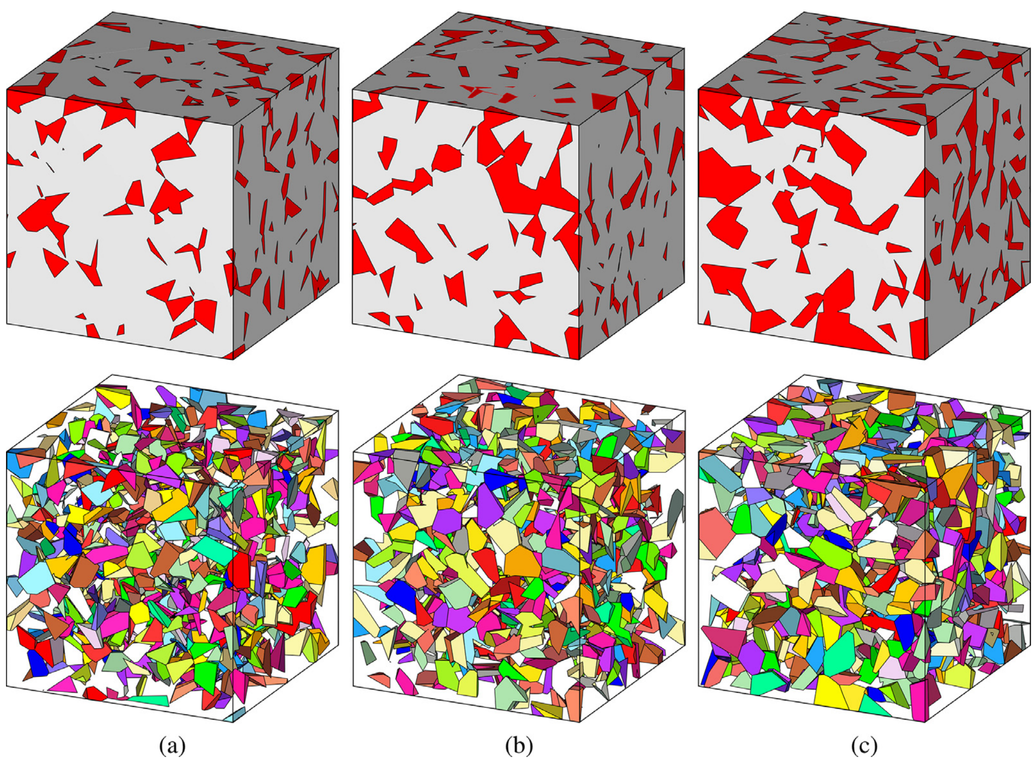

Fig. 3. Representative elementary volumes with different binder volumetric fractions: (a) 7.5%, (b) 10%, and (c) 15%. Volumes contain 1000 WC grains and 1000 binder pools (top images show binder in red, bottom images show only binder pools). (For interpretation of the references to color in this figure legend, the reader is referred to the web version of this article.)

where coefficient D_i^d and D_i^s are the material parameters of ith phase acting on deviatoric and spherical parts of $\boldsymbol{\beta}_i$ denoted by $\boldsymbol{\beta}_i^{\mathrm{dev}}$ and $\boldsymbol{\beta}_i^{\mathrm{sph}}$, respectively, and used to control the non-linearity of the stress redistribution. Four parameters D_i^* are calibrated using results of the FE simulation of the corresponding composite. The value of $\boldsymbol{\beta}$ is deduced from the $\boldsymbol{\beta}_i$ by using the fact that the average of the local stresses is nothing but the macroscopic stress:

$$\boldsymbol{\beta} = \langle \underset{\sim}{\mathrm{A}}_i : \underset{\sim}{\mathrm{C}}^{\star} \rangle^{-1} : \langle \underset{\sim}{\mathrm{A}}_i : \underset{\sim}{\mathrm{C}}^{\star} : \boldsymbol{\beta}_i \rangle \tag{13}$$

The iterative scheme for obtaining the effective elasticity tensor is as follows:

$$\underset{\sim}{\mathrm{C}}_{\mathrm{eff}k} = \sum_{i=\mathrm{WC,B}} \eta_i \underset{\sim}{\mathrm{C}}_i : \left[\underset{\sim}{\mathrm{I}} + \underset{\sim}{\mathrm{S}}_{k-1} : \left(\underset{\sim}{\mathrm{C}}_{\mathrm{eff}_{k-1}}^{-1} : \underset{\sim}{\mathrm{C}}_i - \underset{\sim}{\mathrm{I}} \right) \right]^{-1}, \tag{14}$$

where k is the iteration counter. The initial guess of the effective elasticity tensor $\underset{\sim}{\mathrm{C}}_0$ for the two-phase composite is taken as:

$$\underset{\sim}{\mathrm{C}}_{\mathrm{eff}0} = \eta_1 \underset{\sim}{\mathrm{C}}_1 + (1 - \eta_1) \underset{\sim}{\mathrm{C}}_2. \tag{15}$$

The elasticity tensors $\underset{\sim}{\mathrm{C}}_1$ and $\underset{\sim}{\mathrm{C}}_2$ are those of the binder and the WC materials. They are isotropic and constructed using the parameters E_{WC}, ν_{WC}, E_B and ν_B.

3.3. Impact simulation

We are particularly interested in the mechanical behavior of WC hardmetal under loads, which are representative for rock drilling, when a drill-bit insert impacts the rock. The drill-bit operates in rotary-percussive regime: 2000–3000 hits/min and 50–150 rpm. The real shape of the hardmetal inserts can be properly approximated by a paraboloid, which fits perfectly the Hertz's contact theory (Hertz, 1988), and which, for relatively small contact radius, is indistinguishable from a spherical shape, which was used in the present study.

To improve the design of drill-bits and to enhance wear resistance of drill-bit inserts, it is crucial to understand what is causing an increase in material loss. The issue of drill-bit wear and efficiency is an active research topic, where challenges come from

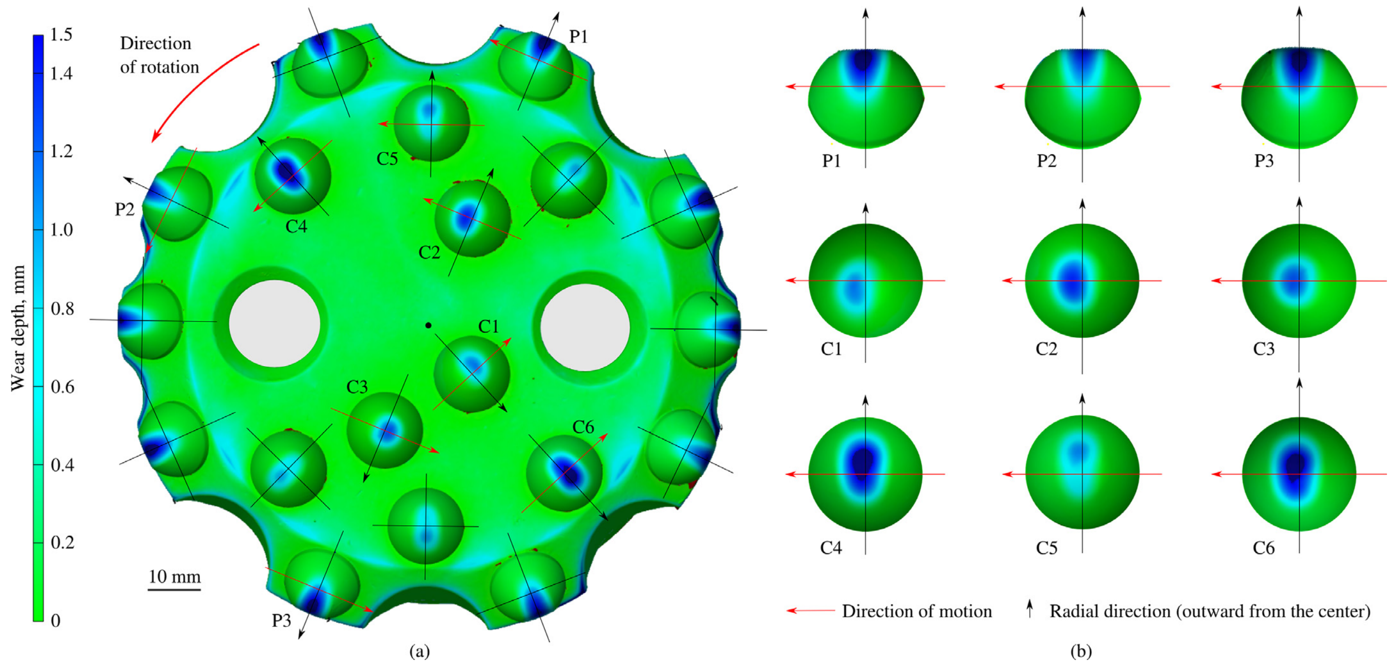

Fig. 4. Wear pattern on a drill-bit after 80 m drilled through hard rock formation: (a) general view, (b) zoom on several central ("C") and peripheral ("P") inserts. Red arrow shows the direction of insert's motion with respect to the rock, black arrow denotes the outward direction from the center of rotation of the drill-bit. For the central inserts the two lines cross on their centers. The distance from the center d for the considered inserts are as follows: C1 $d \approx 12.4$ mm, for C2-C3 $d \approx 21.5$ mm, for C4-C6 $d \approx 37.9$ mm. (For interpretation of the references to color in this figure legend, the reader is referred to the web version of this article.)

the fact that many factors come into play in drilling. However, despite the varying configuration and composition of drill-bits used in rotary-percussive drilling, a common pattern of insert's wear traces can be found. Indicative results were presented in an experimental study (Tkalich et al., 2017b), where the full-scale rotary-percussive drilling in hard rock was performed, with an average rotation speed of 80 rpm, feed force of 4.3 kN, and percussion frequency of 65 Hz. The wear traces on all the drill-bit inserts exhibited inclination towards the insert's leading edge (the results are recalled in Fig. 4). This can be explained by the harmful tensile stresses present on the leading edges of inserts due to the frictional contact with rock. The higher the impact angle is, the greater is the induced tensile stress. Impact angle is zero at the very center of drill-bit rotation and increases towards the periphery. Additionally, the angle is altered by the roughness and the shape of the bore hole floor. In the current study, with the help of numerical tools we focus on this single insert–rock interaction aspect - the effect of the impact angle. In order to demonstrate how the tangential forces change the response of the WC hardmetal inserts to the impact, we compare the normal and the oblique insert–rock impacts, both employing the same simple model geometry.

We use the finite-element method to solve an insert–rock contact problem at the macroscopic scale for normal and mixed normal/tangential contacts. Impact simulations are performed using Z-set finite element software suite (Besson and Foerch, 1997; Z-set, 2017) in a quasi-static framework, where the impactor (half sphere) comes in frictional contact with a rock mass cylinder (see Fig. 5). Impactor is driven by displacements imposed on its top (hatched face in Fig. 5):

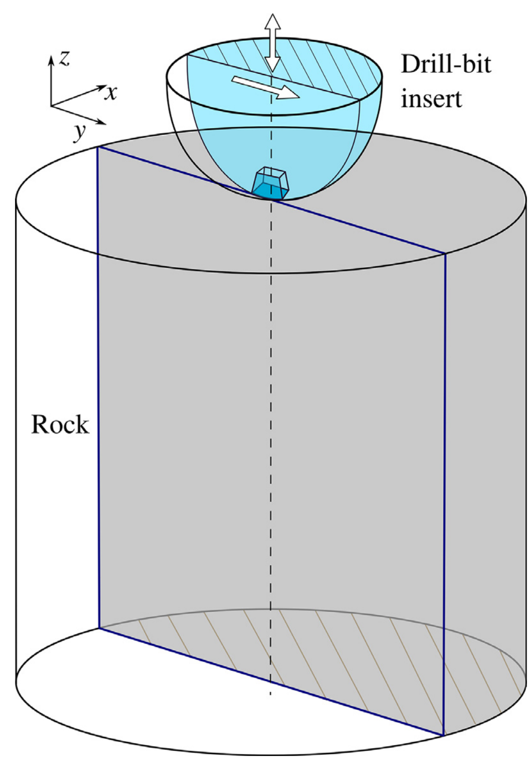

Fig. 5. Illustration of the macroscopic impact geometry.

$$\begin{cases} u_x = 0, \\ u_y(t) = u_0 \tan(\theta) t/t_0, \\ u_z(t) = -u_0 g(t); \end{cases} \text{ with } g(t) = \begin{cases} t/t_0, & \text{if } 0 \le t < t_0, \\ 1 - (t - t_0)/t_0, & \text{if } t_0 \le t < 2t_0. \end{cases} \quad (16)$$

In simple words, the impactor hits the rock surface at angle θ ($\theta = 0$ corresponds to the normal impact), in the interval $0 < t < t_0$ the indenter moves towards the surface, and for $t_0 \le t < 2t_0$ it moves outwards. The maximal penetration is $u_0 = 1$ mm. The trajectory angle with the rock surface normal is the same for loading and unloading. Dimensions of the rock are chosen large enough to avoid edge effects (depth 15 mm, diameter 20 mm), insert's radius is 5 mm. The rock block is fixed in all directions at its bottom

Table 2
Proportional stress paths in terms of principal stresses used to compute the effective behavior and the yield surface; σ_0 is an arbitrary normalization stress.

	T5	T4	T3	T2	T1	S	C1	C2	C3	C4	C5	C6	C7	C8
σ_1/σ_0	1	1	1	1	1	−1	−1	−1	−1	−1	−1	−1	−1	−1
σ_2/σ_0	1	0.85	0.65	0.35	0	0.5	0	−0.4	−0.6	−0.73	−0.81	−0.88	−0.94	−1
σ_3/σ_0	1	0.85	0.65	0.35	0	0.5	0	−0.4	−0.6	−0.73	−0.81	−0.88	−0.94	−1

and outer surfaces. At the symmetry plane, a symmetry boundary condition is used imposing zero normal displacement. Approximately 200 000 elements and 41 000 nodes were used to mesh the model: 8-node linear brick and 6-node linear prism elements with full integration are used, the mesh is dense in the zone of the interest near the impact. Surface mesh in the impact zone form a regular quadrilateral grid as seen in Fig. 11. Coulomb's friction law is used in the interface with friction coefficient $\mu = 0.3$, which is an average macroscopic friction value for interactions consisting of abrasive crushed rock surface and particles, combined with lubricants which are used in drilling (Beste and Jacobson, 2002).

We use β-model for the WC hardmetal, integrated at every Gauss-point of the impactor. Parameters D_i^* for the β_i evolution are calibrated on finite element simulations of the synthetic microstructure under proportional loadings, see Section 4.1. Linearly elastic material is used for the rock with Young's modulus $E_R = 79$ GPa and Poisson's ratio $\nu_R = 0.26$, which corresponds to Kuru granite elastic properties (Tkalich et al., 2016). No damage, fracture or fragmentation is introduced. This choice is partly justified by the fact that at high confining pressure the compressive strength of the granite significantly increases and it can bear rather high loads (Hokka et al., 2016). On the other hand, in drilling application the rock crashes by chipping (big pieces) and fragments into powder in the zone right beneath the impactor. Thus, in forward motion the rock should also experience a softening behavior as well as during unloading. Because of huge irreversible rock deformation/crushing, the stresses in the tool might drop abruptly and possibly do not present such high friction induced shear components. Nevertheless, our simulations offer insights into the stress heterogeneity within the WC hardmetal bulk, especially for the material near the outer surface of the insert. The stress state is analyzed in one-element thickness layer near the contact surface, at which wear of the real inserts occurs. At the microstructure scale the wear can be seen as an accumulation of micro-fractures of WC grains and other damage mechanisms, which occur only near the surface as was confirmed by microscope observations using scanning electron microscope (Beste et al., 2001; Olovsjö et al., 2013; Tkalich et al., 2017b).

4. Results

4.1. Effective behavior

The effective elastic moduli and initial yield surface of WC hardmetal on a macro-scale are determined by means of series of FE simulations with proportional loadings applied on hardmetal RVEs. A mixed loading type is applied, with a zero normal displacement on three adjusted sides of the cube-shaped RVE (see Fig. 2): $u_x = 0$ at $x = 0$ plane, $u_y = 0$ at $y = 0$ and $u_z = 0$ at $z = 0$; the other three faces are loaded with normal tractions. The stress paths are shown in Fig. 6, and description in terms of applied principal stresses is given in Table 2. Stresses and strains in both phases are given directly in the β-model by Eqs. (7) and (8), whereas in FE model the average response of each phase is calculated as the volume average of the corresponding phase. The average values are computed in an internal volume (see Fig. 2d) to avoid edge effects. Volume fraction of phases in the 75% internal volume is the same as in the total RVE. Material parameters for each phase are given in Table 1. The β-model was calibrated using the results of these simulations and the following parameters were chosen: $D_1^d = 200$, $D_1^s = 50$, $D_2^d = 30$ and $D_2^s = 30$ (see Eq. (12) for reference).

Table 3
Effective Young's moduli and Poisson's ratios for each microstructure obtained using FE and UF models, and the relative error.

Binder [vol.%]	Young's modulus, E_{eff} [GPa]			Poisson's ratio, ν_{eff}		
	FE	UF	Δ[%]	FE	UF	Δ[%]
7.5	656.6	651.8	0.7	0.204	0.204	< 0.1
10.0	638.9	633.7	0.8	0.206	0.207	0.5
15.0	598.8	598.2	0.1	0.211	0.212	0.5

For a model consisting of 200 WC grains and 200 binder pools, no significant difference in effective behavior was found between models with different morphology realizations. This is a validation of the fact that the RVE size is big enough to be representative. Experimental studies, for instance by Doi et al. (1970) or Koopman et al. (2002), report that elastic moduli of the hardmetal depend only on the volume fraction of the phases, for the conventional composites (binder 5–20 vol.%). The elastic moduli obtained with FE and UF models are compared in Table 3 for various amount of binder phase, between 7.5 and 15%. A good agreement is found with the relative error being lesser than 1 %. These results are consistent with previously reported data (Tkalich et al., 2017a, see Table 8).

Figs. 7–9 show the stress-strain curves obtained using FE and UF models for a single realization of the microstructure with the binder volume fraction of 10%. For the sake of brevity, only three loadings are shown: "T4", "S" and "C2", that respectively correspond to asymmetric triaxial tension, pure shear and asymmetric triaxial compression. Three curves are plotted for each loading, which correspond to the effective, average WC and average binder behaviors. The macroscopic curve is rather close to the curve of the WC phase, due to the small volume fraction of the binder. Depending on the loading type, the plastic strain is larger in the WC phase (case of T4 loading) or in the binder (cases of S and C2 loadings). This is consistent with the fact that plastic yield in tension is much smaller than in compression for WC phase, and that the elastic stiffness is larger for WC than for the binder. The general agreement between the reference finite-element model and the uniform field model is acceptable. The best fit is obtained for the pure shear case, meanwhile, for the two other cases, the binder's response in the UF model is too soft, however, it does not affect significantly the macroscopic response.

The so-called "equi-loading" lines link points on the three curves (effective, WC, and binder) at the same loading step. This offers the opportunity to examine the type of redistribution. A pure elastic redistribution, as in Kröner's model, would present a constant slope of the equi-loading line, depending on elastic moduli only. In the present model, the slope decreases with increasing plastic strain, as classically observed for self-consistent models. Again, it can be observed that the best agreement is obtained for pure shear. The slope-change predicted by the UF model is too slow for the tensile case, and too fast for the compressive case.

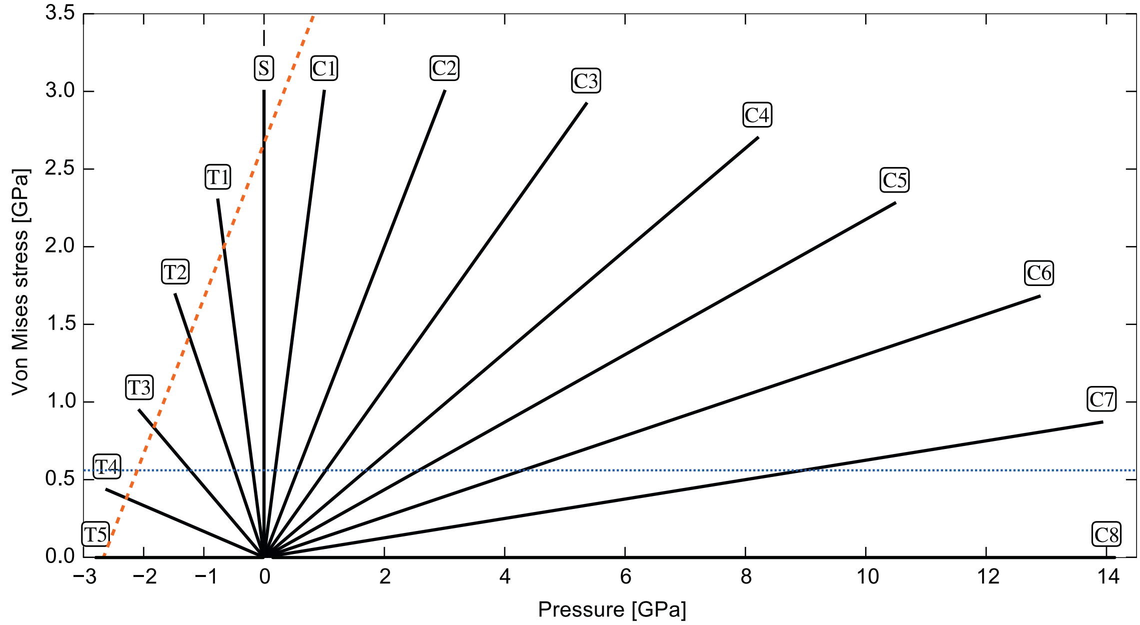

Fig. 6. Proportional loading paths used to determine effective elastic and plastic behavior. Description of each path in terms of applied principal stresses is given in Table 2. Dashed red line denotes the WC yield surface, and dotted blue line - the binder yield surface. (For interpretation of the references to color in this figure legend, the reader is referred to the web version of this article.)

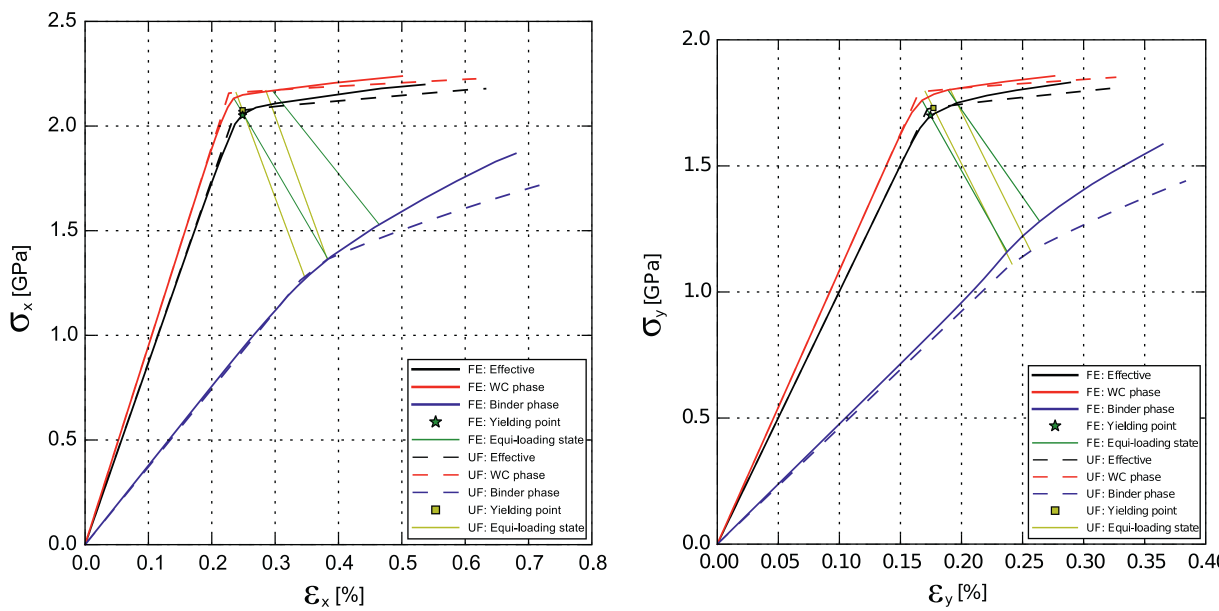

(a) (b)

Fig. 7. Stress-strain curves for model with 10% of the binder under asymmetric triaxial tensile loading ("T4"-type in Table 2 and in Fig. 6) obtained using FE and UF models. Deformation curves are presented in (a) "*x*" and (b) "*y*" directions.

The yield stress for each type of loading was identified as the point at which the effective equivalent plastic strain $\bar{p}$ reaches 0.01%, which is computed as

$$\bar{p} = \sqrt{\frac{2}{3}\boldsymbol{E}^p : \boldsymbol{E}^p}\,, \tag{17}$$

where $\boldsymbol{E}^p$ is the effective plastic strain tensor, which is computed as follows, using effective stress ($\boldsymbol{\Sigma}$) – effective strain ($\boldsymbol{E}$) curves:

$$\boldsymbol{E}^p = \boldsymbol{E} - \underset{\sim}{\mathrm{C}}_{\mathrm{eff}}^{-1} : \boldsymbol{\Sigma}\,. \tag{18}$$

The yield stresses obtained using FE simulations and the UF model and shown in Fig. 10 in pressure–von Mises stress space. Unlike the case of the effective elastic properties, the results depend now on the chosen morphology. Five RVE models are selected for each of the three binder content cases to perform the FE simulations. The scatter in yield stresses determined using FE simulations is considerable, especially when the pressure is positive, whereas almost no scatter is found when it is negative. Dirichlet boundary conditions were used, which are responsible for small deviation of the average stress states from the stress paths.

Expectedly, at positive pressures the yield surfaces predicted by the FE model is rather different from those by the UF model. This is because no plasticity can appear in Eshelby's inclusion problem

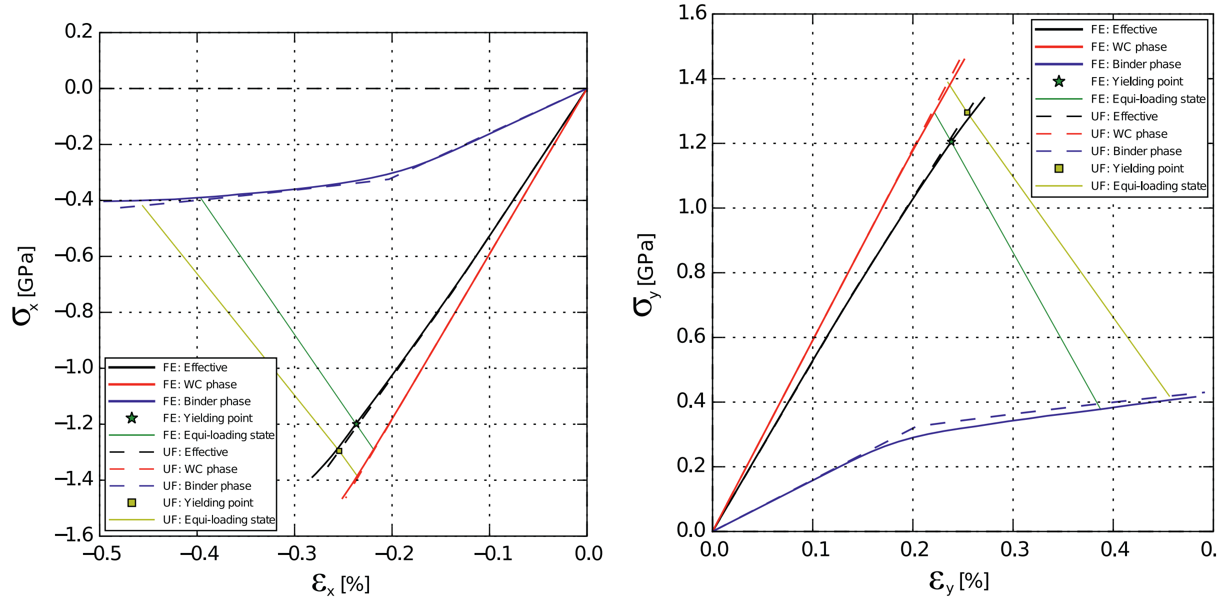

(a) (b)

Fig. 8. Stress-strain curves for model with 10% of the binder under shear loading ("S"-type in Table 2 and in Fig. 6) obtained using FE and UF models. Deformation curves are presented in (a) "x" and (b) "y" directions.

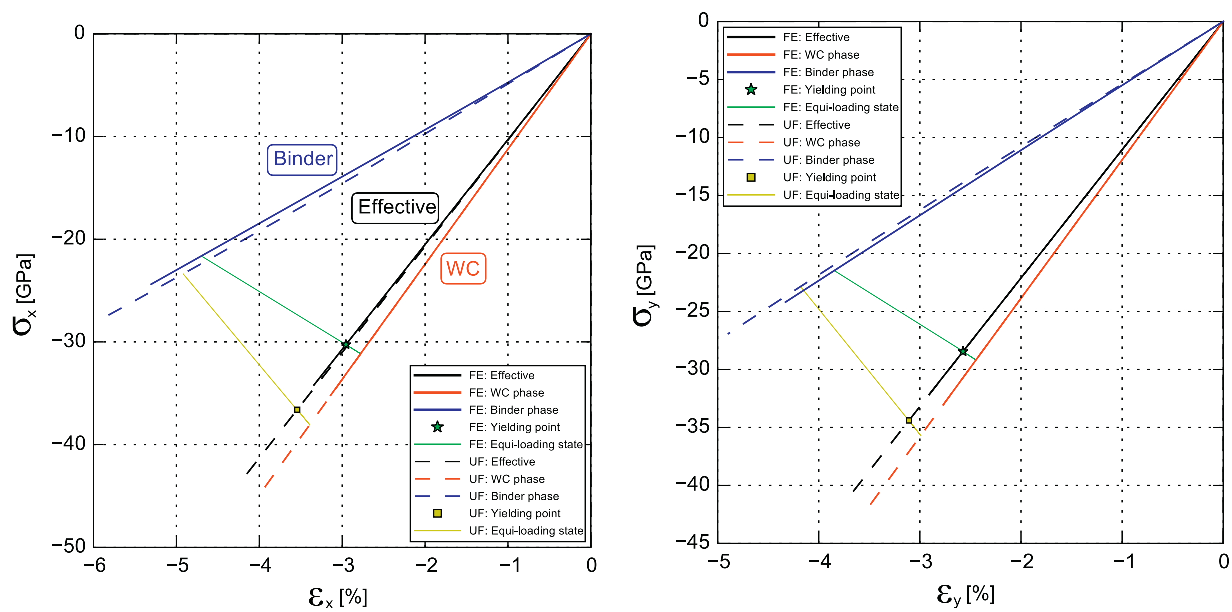

(a) (b)

Fig. 9. Stress-strain curves for model with 10% of the binder under asymmetric triaxial compression loading ("C2"-type in Table 2 and in Fig. 6) obtained using FE and UF models. Deformation curves are presented in (a) "x" and (b) "y" directions.

under hydrostatic pressure, whereas in FE model stresses redistribute due to morphological nuances of the microstructure, which result in plastic flow in the binder. Thus, the true yield surface forms a curve with two branches: (i) Drucker–Prager-type branch, at which von Mises yield stress increases linearly with the pressure with the friction angle almost equivalent to the friction angle of WC, this branch is well predicted by the UF model; the maximal von Mises yield value predicted by the UF model slightly underestimates the FE result, in the worst case of 7.5% of binder it predicts a 10% lower value; (ii) Cap-branch, at which von Mises yield stress decreases down to zero under increasing pressure. In the current study we do not analyze the plastic strain tensor evolution, and thus the macroscopic plastic flow rule remains undetermined and the model incomplete. The stress state with a high hydrostatic pressure is of high importance for insert–rock interaction analysis, as near the contact surface huge pressures develop. In this study, however, we limit the macroscopic description of cemented WC to this provided by the β-model, bearing in mind that a more accurate macroscopic model can be used in future studies.

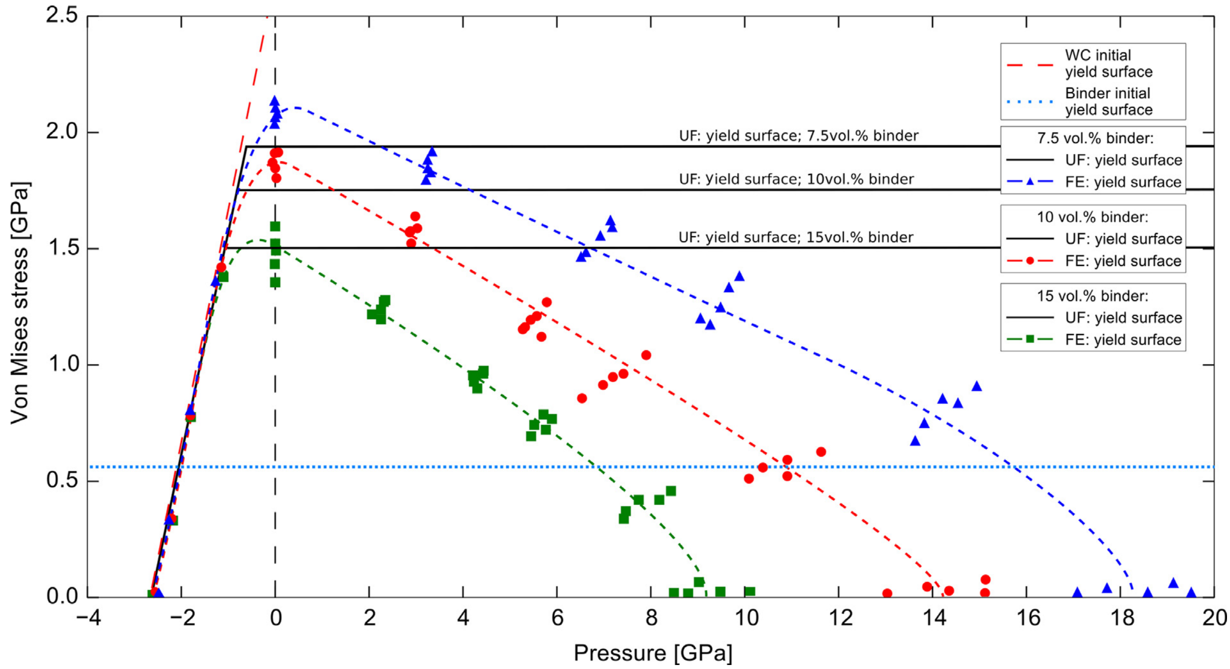

Fig. 10. Initial yield surfaces for WC hardmetal, determined using UF and FE models for 10% of volumetric binder fractions. Initial yield surfaces of the WC and the binder phases are also plotted for the sake of comparison.

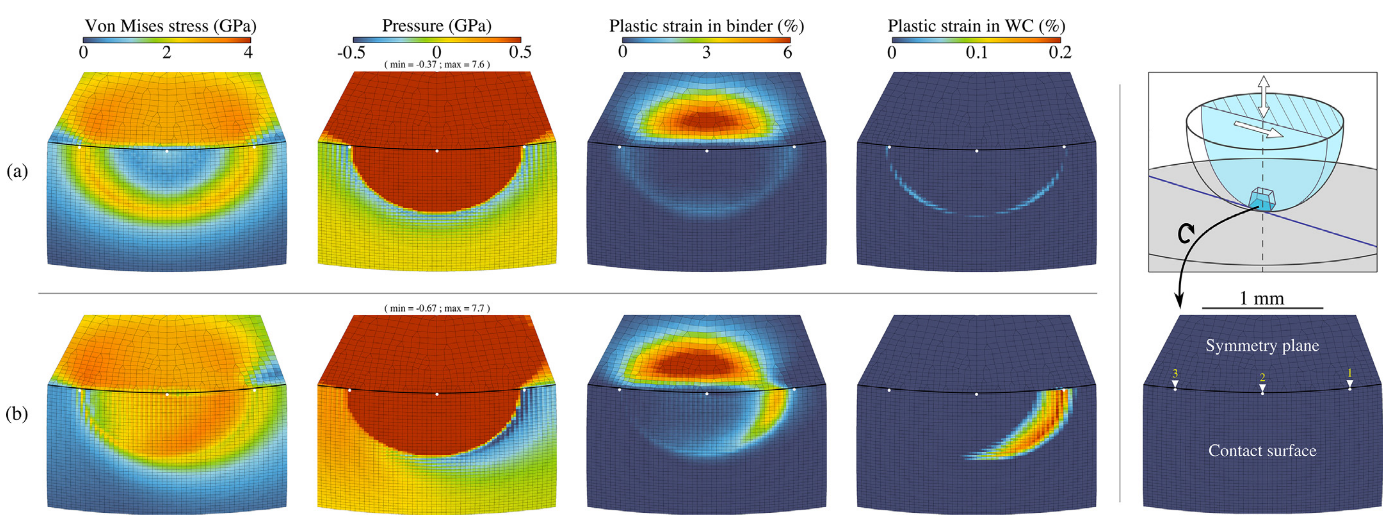

Fig. 11. Stress and plastic strain fields in hardmetal impactor, at the time of the maximal penetration in the cases of (a) normal (vertical) and (b) 15 ° oblique impacts. Only a part of the impactor is shown, rock is not shown.

4.2. Representative loadings

Two macroscopic quasi-static impact simulations were performed: a normal (vertical) and an oblique impact at $\theta = 15^\circ$. We recall that the calibrated β-model is used for WC hardmetal, a linear-elastic model is used for the rock.

For the case of normal impact, the stress state corresponds to a normal frictional contact with a “slip-ring” and sticking center zones in the contact (Johnson, 1987). Plastic slip is developed in WC phase around the contour of the maximal extension of the contact area, and is marginal compared to plastic strains in binder. However, right outside the contact zone the axial stress σ_{rr} is negative, but is compensated by positive $\sigma_{\theta\theta}$ resulting in zero hydrostatic pressure and pure shear stress state outside the contact area, where yield in WC phase might occur. Within the slip-ring at the periphery of contact zone $s \le r \le a$, where s is the stick-zone radius and a is the contact radius, the stress state has a shear component, proportional to the contact pressure $|\sigma_{rz}| = \mu\,|\sigma_{zz}|$, with coefficient of friction μ.

For the case of oblique impact, the stress state corresponds mainly to a full slip frictional sliding (Hamilton and Goodman, 1966) at which strong tensile stress component develops in front of the contact zone resulting in negative hydrostatic pressure (see Fig. 11b). This zone becomes favorable for plastification/microfracturing of WC phase (see Fig. 11d). An increase in the friction coefficient would lead to even higher magnitudes of the in-plane stress component σ_{yy}, which is collinear with the impact inclination. The resulting plastic zone is crescent shaped, that could represent a failure limit for a possible material “chipping”. Fig. 11 demonstrates the von Mises stress distribution in WC phase as well as plastic strain accumulated in binder and in WC.

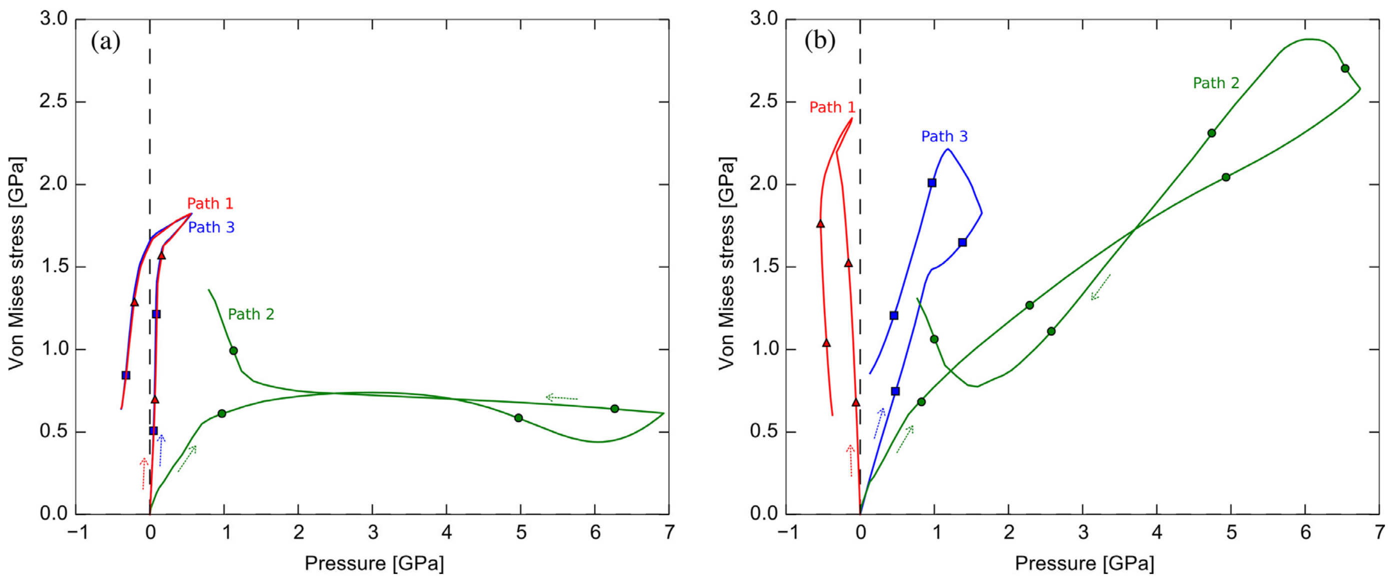

Fig. 12. Stress history paths extracted from three locations on the impactor's contact surface. Paths from the (a) normal and (b) 15° oblique impact simulations. The path numbers correspond to the locations in Fig. 11.

To analyze the stress evolution in detail, three locations on the impactor's contact surface were selected, see points marked with numbers 1–3 in Fig. 11. Stress history paths extracted from those locations are plotted in pressure–von Mises stress space in Fig. 12, and are marked with the numbers corresponding to the locations in Fig. 11. In the simulations that follows, we employ paths 1 and 2 as Neumann boundary conditions for the WC hardmetal finite-element 3D RVE model. Paths are applied on the sides of the cube-shaped RVE in a form of a full strain tensor.

The responses of the RVE to four representative loading paths are shown in Fig. 13: paths 1 and 2 from both the normal and the oblique impacts. Curves in Fig. 13 are showing the RVE's total, WC and binder phase's "microscopic mean". Note that since the pressure is a linear combination of stress components, the macroscopic and microscopic averaged values are the same, which is not the case for the von Mises stress being a non-linear function of stress components. That is the reason why the mean microscopic paths in Fig. 13 do not coincide with macroscopic ones shown in Fig. 12. The means were obtained in two steps in the following order: first, the value of von Mises stress and pressure was computed for each Gauss point, and second, the weighted average was calculated by taking into account the volume corresponding to each point. In order to avoid possible edge effects, the data was extracted only from the 75% of the inner RVE volume. For the moments of maximal penetration, the dispersion of stresses in each phase is shown in Fig. 13 in a form of joint stress probability densities ("clouds") in pressure–von Mises stress space. The clouds give an important insight on the state of the RVE. While the mean values could remain remote from the inelastic domain, clouds are able to give information about the number of material points that have reached the plastic domain. Thus, the dispersion clouds give information regarding the possible accumulation of plastic deformation or microfractures within the material bulk.

In the case of path 2 from both the normal [Fig. 13a.2] and the oblique [Fig. 13b.2] impacts, during the whole loading cycle the entire WC phase remains elastic, whereas the stress in the binder rapidly reaches the initial yield stress and the hardening takes place. However, the plastic strain in binder remains relatively small, as the hardening is significant. WC cloud show dispersion in pressure of about 2 GPa, and slightly higher - about 2.5 GPa in the von Mises stress. Shape of the binder cloud is elongated more along the pressure axis spreading for about 2.5 GPa, while only for about 0.6 GPa along the von Mises axis since the stress is bounded by its saturated value $J_2^{\max}(\boldsymbol{\sigma}_B) = R_{B_0} + Q_B \approx 1.17$ GPa.

In the case of path 1 from both the normal (Fig. 13a.1) and the oblique (Fig. 13b.1) impacts, elastic limits are reached in both phases. Higher von Mises stresses and developed tensile stresses lead to greater levels of plastic deformation accumulated in WC grains. Due to brittle nature of WC grains, plastic strains generated at negative pressures represent grains' fracturing in real hardmetal, which would lead to an increased rate of insert's surface deterioration, i.e. wear. The clouds' shapes in the case of the normal impact resembles that for the path 2, however, they are about 1.6 times smaller in size along both axes. In the case of the oblique impact, WC cloud gets heavily distorted due to the material's post-yield behavior. The fact that flow potential normal is inclined in the pressure-von Mises stress space (dilation angle $\psi_{\mathrm{WC}} = 30°$) leads to the cloud distortion following that normal. Behavior of the binder phase is affected by the increase in negative pressure, which results in the increase of the binder cloud.

Resulting plastic strain fields at the maximal penetration are shown in Fig. 14 for locations (paths) 1 and 2 for the normal and oblique impacts, where the RVE is split in two parts along grain boundaries. Equivalent plastic strain variables are stored separately for WC and binder phases, which allows to illustrate them distinctly within the microstructure bulk. Plasticity near the outer RVE boundaries is induced by boundary conditions and should be disregarded. Majority of the binder material has reached the state of inelastic behavior in all cases, since high shear stresses induced within the microstructure. It can be also seen in "clouds" in Fig. 13. In the case of the normal impact, inelastic deformation in WC grains is very marginal and can be observed only at location (path 1) concentrates at corners near interfaces with the binder [see Fig. 14c]. For the oblique impact, contrary to the prediction of β-model (compare plastic strain levels at point 1 in Fig. 11) the plastic strain in WC grains is comparable with that in the binder. In the case of path 2 loading, the combination of very significant hydrostatic stresses and relatively low shear stresses prevent the WC grains from reaching the elastic limit. Thus, the hardmetal's surface at the location corresponding to path 2 (point 2 in Fig. 11) is much less prone to wear, compared to that at the dangerous location 1 (point 1 in Fig. 11).

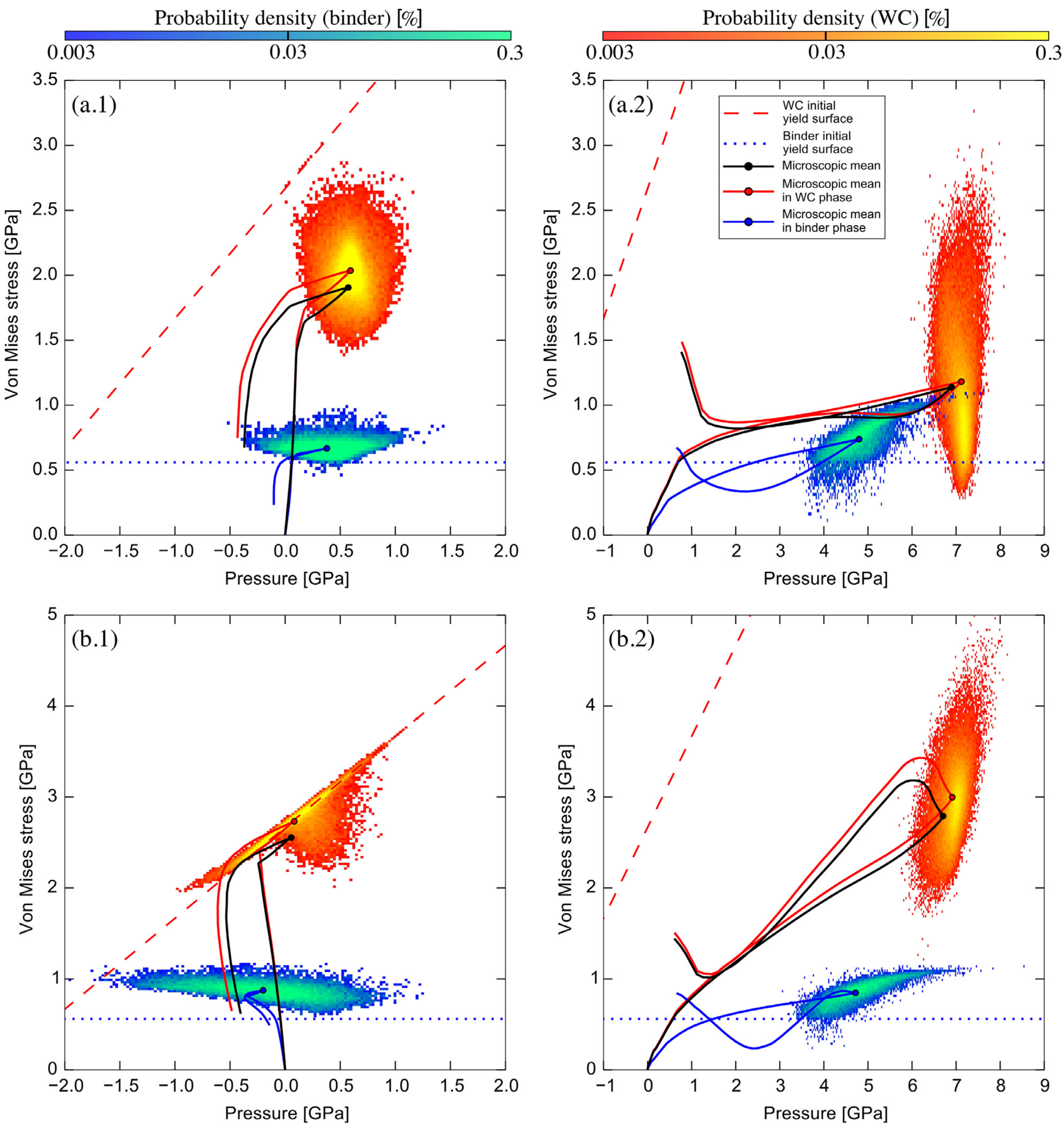

Fig. 13. The responses of the RVE to four representative loading paths: (a.1) paths 1 and (a.2) path 2 from the normal impact, and (b.1) path 1 and (b.2) path 2 from the 15° oblique impact. "Microscopic mean" are shown for RVE's total, WC and binder phases. or the moments of maximal penetration, the dispersion of stresses in each phase is shown in a form of joint stress probability densities ("clouds") for both hardmetal phases. Color-bars show the probability to find a point at a current location in stress space (logarithmic color scale). The size of each "bin" in the cloud is 25 × 25 MPa^2.

5. Conclusions

5.1. Summary

The three-step strategy employed in the current study had its goal in obtaining the distribution of stresses and strains within the WC hardmetal bulk, which occurs under loadings, representative for the rotary-percussive drilling. Within the undertaken investigation we computed effective elastic moduli and determined effective initial yield surface for the WC hardmetal composite with different binder content.

Two homogenization methods were used: (i) a full-field model based on a direct 3D finite-element simulation of synthetic microstructure-respective models, where a new algorithm based on the Voronoi tessellation has been developed and used to construct a two-phase two-interface microstructure; (ii) a β-model, which is a nonlinear extension of the self-consistent Kröner's model. Each constituent is represented by its own material model, namely classical J2 plasticity for the binder, and a Drucker–Prager model for the WC phase.

The effective elastic behavior predicted by the UF model follows very closely with that determined using FE models. Outside the elastic domain, the UF model is also able to accurately predict

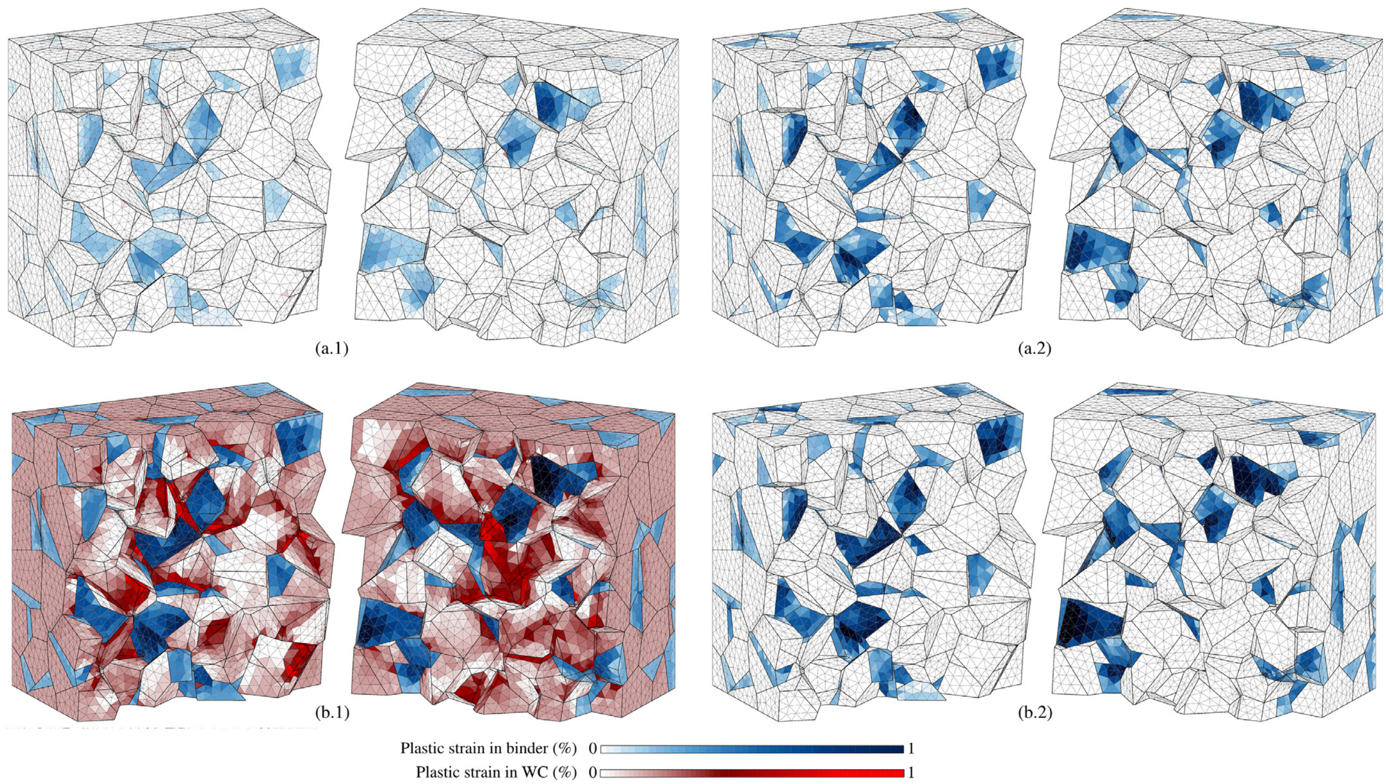

Fig. 14. Plastic strain distribution in WC and binder phases at the moment of the maximal penetration along the representative loadings: (a.1) path 1 in the normal impact; (a.2) path 2 in the normal impact; (b.1) path 1 in the oblique impact; (b.2) path 2 in the oblique impact.

the behavior of the pressure-dependent WC hardmetal for moderate loads. The initial yield surface for WC hardmetal obtained with the full-field 3D finite-element model consists of two distinguishable branches in the "pressure–von Mises" stress space: a linear pressure-dependent segment in a part of tensile hydrostatic stresses and a "cap"-shaped segment in a part of compressive hydrostatic stresses. The uniform field model predicts a yield surface which consists of a linear pressure-dependent first branch and the second branch in the part of compressive hydrostatic stresses - parallel to the pressure axis. No "cap"-shaped segment is present here, since the UF model cannot capture the dispersion of stresses around the mean value, which are responsible for reaching the plastic limit in the full-field model. For predicting extreme phenomena like wear and fracture, which are governed not by mean stress values but rather by the tail of the probability distributions, a more sophisticated and accurate homogenization model is needed (see, e.g., recent works (Fritzen and Leuschner, 2013; Michel and Suquet, 2016)).

Performed finite-element simulations of macro-scale impacts employing β-model for the WC hardmetal impactor provide a stress evolution paths, which are regarded as representative loadings for the hardmetal at a scale of its representative volume element. This analysis enables to reveal microscopic stress states, which can extend far from the mean values predicted by the β-model. It is important to remark here that in the center of the contact zone in absence of sliding a high hydrostatic compression rules: as we saw the UF model cannot predict any plastic yield for such a load, that what is observed in Fig. 11, third column top row. In the presence of a sliding component (oblique impact), shear tractions appear in the interface and result in some plastic activity in the binder (see Fig. 11, third column lower row). On the contrary in the microscopic full-field analysis a different picture emerges. See the "cloud" and the microscopic mean curve for the binder in Fig. 13a.2 corresponding to the central point (path 2) microscopic state for the normal impact: a considerable plastic strain developes in almost whole binder phase. It is important to bear in mind this example especially for the contact/impact microstructral analysis, which frequently promotes high hydrostatic stresses near the contact interface.

5.2. Implications for wear of drilling tools

In rotary-percussive drilling, drill-bit inserts impact the rock surface at various angles. Impact angle is zero at the very center of rotation of the drill-bit and increases towards the edges. This angle however can be altered by the topography of the bore hole floor. Due to friction, higher impact angles result in greater tensile stresses induced on the leading edges of inserts. Since WC grains are weak under tensile stresses, this region is prone to microfracturing of grains with its subsequent removal, which leads to the macroscopic wear. Microstructural analysis, made possible by the three-step multiscale strategy, demonstrates that macroscopic zones at the leading edges of the inserts are the critical locations for the near-surface microfracture of WC grains in tensile mode. This result correlates with experimental observations (Tkalich et al., 2017b): (1) the wear rate increases with the increasing distance of drill-bit inserts from the center; (2) the wear is deeper on the leading edges of inserts. Experimental study by Swick et al. (1992) showed no traces of abrasive scratches on worn surfaces, which correlates with the finding that the abrasive wear occurs on the material with lower melting temperature (Bowden and Tabor, 2001). Thus the abrasive should not happen on the hardmetal since the melting temperature of WC is higher than those of rock constituents. Therefore, we can conclude that the tensile stresses occurring on leading edges of drill-bit inserts due to frictional oblique impact can play a significant role in WC grain fracturing which promotes wear.

Acknowledgment

We would like to acknowledge the support from The Research Council of Norway and their industrial consortia through the knowledge building project (grants NFR 216436 and NFR 254984). We are also grateful to Nikolay Osipov for his valuable help with finite-element simulations. Helpful wear patterns data was provided by Maria Bengtsson from LKAB Wassara, which is highly appreciated. We would like also to thank in-depth remarks and suggestions of the anonymous reviewer.

References

Almond, E., Roebuck, B., 1988. Identification of optimum binder phase compositions for improved WC hard metals. Mater. Sci. Eng.: A 105, 237–248.
Barbe, F., Decker, L., Jeulin, D., Cailletaud, G., 2001. Intergranular and intragranular behavior of polycrystalline aggregates. part 1: FE model. Int. J. Plast. 17 (4), 513–536.
Besson, J., Cailletaud, G., Chaboche, J.-L., Forest, S., 2009. Non-Linear Mechanics of Materials. vol. 167. Springer Science and Business Media.
Besson, J., Foerch, R., 1997. Large scale object-oriented finite element code design. Comput Methods Appl Mech Eng 142 (1), 165–187.
Beste, U., Hartzell, T., Engqvist, H., Axén, N., 2001. Surface damage on cemented carbide rock-drill buttons. Wear 249 (3), 324–329.
Beste, U., Jacobson, S., 2002. Friction between a cemented carbide rock drill button and different rock types. Wear 253 (11), 1219–1221.
Beste, U., Jacobson, S., 2008. A new view of the deterioration and wear of wc/co cemented carbide rock drill buttons. Wear 264 (11), 1129–1141.
Bowden, F.P., Tabor, D., 2001. The Friction and Lubrication of Solids. vol. 1. Oxford university press.
Budiansky, B., WU, T. T., 1961. Theoretical prediction of plastic strains of polycrystals. Technical report, DTIC Document, DTIC.
Cailletaud, G., Coudon, F., 2015. Materials with Internal Structure. Multiscale and Multifield Modeling and Simulation. In: Ch. Scale Transition Rules Applied to Crystal Plasticity. Springer, pp. 1–16. ISSN 2195-9862, 2195-9870 (electronic) ISBN 978-3-319-21493-1; 978-3-319-21494-8 (eBook)
Cailletaud, G., Pilvin, P., 1994. Utilisation de modèles polycristallins pour le calcul par éléments finis. Rev. Eur. des Élém. Finis 3 (4), 515–541.
Csanádi, T., Bl'anda, M., Duszová, A., Chinh, N.Q., Szommer, P., Dusza, J., 2014. Deformation characteristics of WC micropillars. J Eur Ceram Soc 34 (15), 4099–4103.
Doi, H., Fujiwara, Y., Miyake, K., Osawa, Y., 1970. A systematic investigation of elastic moduli of WC–Co alloys. Metal. Mater. Trans. 1 (5), 1417–1425.
Exner, H., 1979. Physical and chemical nature of cemented carbides. Int. Met. Rev. 24 (1), 149–173.
Exner, H., Gurland, J., 1970. A review of parameters influencing some mechanical properties of tungsten carbide–cobalt alloys. Powder Met. 13 (25), 13–31.
Fang, Z.Z., Koopman, M.C., 2014. Cemented tungsten carbide hardmetal – an introduction. In: Sarin, V., Mari, D., Llanes, L. (Eds.), Comprehensive Hard Materials. Volume I. Newnes, pp. 123–138. Ch. 1.04
Fischmeister, H., Schmauder, S., Sigl, L., 1988. Finite element modelling of crack propagation in WC–CO hard metals. Mater. Sci. Eng.: A 105, 305–311.
French, D.N., 1969. X-Ray stress analysis of WC–Co cermets: II, temperature stresses. J. Am. Ceram. Soc. 52 (5), 271–275.
Fritzen, F., Leuschner, M., 2013. Reduced basis hybrid computational homogenization based on a mixed incremental formulation. Comput Methods Appl Mech Eng 260, 143–154.
Gérard, C., Bacroix, B., Bornert, M., Cailletaud, G., Crépin, J., Leclercq, S., 2009. Hardening description for {FCC} materials under complex loading paths. Comput. Mater. Sci 45 (3), 751–755. Proceedings of the 17th International Workshop on Computational Mechanics of Materials IWCMM-17.
Gille, G., Bredthauer, J., Gries, B., Mende, B., Heinrich, W., 2000. Advanced and new grades of WC and binder powder–their properties and application. Int. J. Refract. Met. Hard Mater 18 (2), 87–102.
Golovchan, V., Litoshenko, N., 2010. The stress–strain behavior of WC–Co hardmetals. Comput. Mater. Sci 49 (3), 593–597.
Gurland, J., 1979. A structural approach to the yield strength of two-phase alloys with coarse microstructures. Mater. Sci. Eng. 40 (1), 59–71.
Hall, E., 1951. The deformation and ageing of mild steel: III discussion of results. Proc. Phys. Soc. Lond., Sect. B 64 (9), 747.
Hamilton, G., Goodman, L., 1966. The stress field created by a circular sliding contact. J Appl Mech 33 (2), 371–376.
Hertz, H., 1988. Über die berührung fester elastischer körper. J. für die Reine Angew. Math. 92, 156–171.
Hokka, M., Black, J., Tkalich, D., Fourmeau, M., Kane, A., Hoang, N.-H., Li, C.C., Chen, W.W., Kuokkala, V.T., 2016. Effects of strain rate and confining pressure on the compressive behavior of kuru granite. Int J Impact Eng 91, 183–193.
Huet, C., 1990. Application of variational concepts to size effects in elastic heterogeneous bodies. J. Mech. Phys. Solids 38 (6), 813–841.
Jaensson, B.O., 1971. Residual stresses and stress-strain behaviour of the WC–Co composite material. Mater. Sci. Eng. 8 (1), 41–53.
Johnson, K.L., 1987. Contact Mechanics. Cambridge University Press.
Kanit, T., Forest, S., Galliet, I., Mounoury, V., Jeulin, D., 2003. Determination of the size of the representative volume element for random composites: statistical and numerical approach. Int. J. Solids Struct. 40 (13), 3647–3679.
Koopman, M., Chawla, K.K., Coffin, C., Patterson, B.R., Deng, X., Patel, B.V., Fang, Z., Lockwood, G., 2002. Determination of elastic constants in WC–Co metal matrix composites by resonant ultrasound spectroscopy (rus) and impulse excitation. Adv. Eng. Mater. 4 (1–2), 37–42.
Kröner, E., 1961. Zur plastischen verformung des vielkristalls. Acta Metall. 9 (2), 155–161.
Kröner, E., 1977. Bounds for effective moduli of disordered materials. J. Mech. Phys. Sol. 25, 137–155.
Lee, H.-C., Gurland, J., 1978. Hardness and deformation of cemented tungsten carbide. Mater. Sci. Eng. 33 (1), 125–133.
Lee, M., Gilmore, R., 1982. Single crystal elastic constants of tungsten monocarbide. J. Mater. Sci. 17 (9), 2657–2660.
McHugh, P., Connolly, P., 2003. Micromechanical modelling of ductile crack growth in the binder phase of WC-co. Comput. Mater. Sci 27 (4), 423–436.
Michel, J.C., Suquet, P., 2016. A model-reduction approach in micromechanics of materials preserving the variational structure of constitutive relations. J. Mech. Phys. Solids 90, 254–285.
Nishimatsu, C., 1960. Experimental survey of the deformation of the hard-ductile two-phase alloy system WC-co. Trans. Am. Soc. Metals 52, 469–484.
Olovsjö, S., Johanson, R., Falsafi, F., Bexell, U., Olsson, M., 2013. Surface failure and wear of cemented carbide rock drill buttons –the importance of sample preparation and optimized microscopy settings. Wear 302 (1), 1546–1554.
Pastor, H., 1999. Developments in the powder metallurgy of non-oxide cermets. In: Advanced Science and Technology of Sintering. Springer, pp. 461–474.
Petch, N., 1953. The cleavage strength of polycrystals. J. Iron Steel Inst. 174, 25–28.
Prakash, L., 2014. Fundamentals and General Applications of Hardmetals. In: Sarin, V., Mari, D., Llanes, L. (Eds.), Comprehensive hard materials. Volume I. Newnes, Ch. 1.02, pp. 123–138.
Ramqvist, L., 1965. Wetting of metallic carbides by liquid copper, nickel, cobalt and iron. Int. J. Powder Met. 1 (4).
Roebuck, B., Almond, E., 1988. Deformation and fracture processes and the physical metallurgy of WC–Co hard metals. Int. Mat. Rev. 33, 90–110.
Rycroft, C., 2008. Voro++: a three-dimensional Voronoi cell library in C++. math.lbl.gov/voro++/.
Schedler, W., 1988. Hartmetall für den Praktiker. VDI-Verlag Düsseldorf.
Shackelford, J.F., Han, Y.-H., Kim, S., Kwon, S.-H., 2016. CRC Materials Science and Engineering Handbook. CRC Press.
Shatov, A.V., Ponomarev, S., Firstov, S., 2014. Microstructure and morphology of hardmetals. In: Sarin, V., Mari, D., Llanes, L. (Eds.), Comprehensive hard materials. Volume I. Newnes, Ch. 1.10, pp. 301–344.
Sigl, L., Schmauder, S., 1988. A finite element study of crack growth in WC–co. Int. J. Fract. 36 (4), 305–317.
Swick, K., Stachowiak, G., Batchelor, A., 1992. Mechanism of wear of rotary-percussive drilling bits and the effect of rock type on wear. Tribol. Int. 25 (1), 83–88.
Tkalich, D., Cailletaud, G., Yastrebov, V.A., Kane, A., 2017a. A micromechanical constitutive modeling of WC hardmetals using finite-element and uniform field models. Mech. Mater. 105, 166–187.
Tkalich, D., Fourmeau, M., Kane, A., Li, C.-C., Cailletaud, G., 2016. Experimental and numerical study of kuru granite under confined compression and indentation. Int. J. Rock Mech. Min. Sci. 87, 55–68.
Tkalich, D., Kane, A., Saai, A., Yastrebov, V.A., Hokka, M., Kuokkala, V., Bengtsson, M., From, A., Oelgardt, C., Li, C.C., 2017b. Wear of cemented tungsten carbide percussive drillbit inserts: laboratory and field study. Wear 386, 106–117. http://www.sciencedirect.com/science/article/pii/S0043164816302861
Yastrebov, V., Tkalich, D., Osipov, N., 2018. An augmented Voronoi tesselation algorithm for complex microstructural models.
Z-set, 2017. Z-set: Non-linear material and structure analysis suite. http://www.zset-software.com.